# Role and mechanism of tetrahedral DNA nanostructures in the repair of urethral injury in rats

CAIFEN GUO[1*] and JIAN LI[2*]

[1]Department of Urology, The Affiliated Hospital of Guizhou Medical University, Guiyang, Guizhou 550004, P.R. China;
[2]Department of Sports Medicine, The Beijing Jishuitan Hospital Guizhou Hospital, Guiyang, Guizhou 550014, P.R. China

Received July 29, 2025; Accepted December 18, 2025

DOI: 10.3892/mmr.2026.13815

**Abstract.** Urethral injury is a common type of traumatic damage to the urinary system, often leading to urethral stricture, fibrosis and dysfunction, which significantly impair physiological function and quality of life. The present study aimed to investigate the therapeutic efficacy of the novel immune-regulatory molecule tetrahedral DNA nanostructure (TDN) in a rat model of urethral injury and explore the underlying mechanisms of action. A rat model of urethral injury was established through mechanical injury. Animals were divided into four groups: Control, model, model + rapamycin and model + TDN. Therapeutic effects and associated mechanisms were assessed via retrograde urethrography, Masson's trichrome staining, immunohistochemistry, western blotting, reverse transcription-quantitative PCR (RT-qPCR) and transcriptomic analysis. The results revealed that TDN markedly alleviated the immune response after urethral injury, reduced immune cell infiltration, downregulated the expression of inflammatory cytokines, including IL-6, IL-1β and TNF-α, and effectively inhibited the progression of fibrosis. Masson's trichrome staining and western blotting provided evidence of reduced collagen deposition and decreased expression of fibrosis markers, including α-smooth muscle actin, TGF-β1, collagen I, collagen III and Smad3, after treatment with TDN. Transcriptomic analysis revealed that TDN modulated multiple immune-related pathways, including the NF-κB signaling pathway, NOD-like receptor signaling pathway and cytokine-cytokine receptor interaction, accompanied by a decrease in immune-inflammatory responses, such as reduced inflammatory cytokine production and immune cell infiltration. Additionally, the results suggested that TDN may improve cellular metabolism and inhibit cell proliferation by downregulating the expression of cell cycle-associated genes, as demonstrated by transcriptomic analysis and RT-qPCR validation of cyclin B1, ribonucleotide reductase regulatory subunit M2, polo-like kinase 1 and cyclin-dependent kinase 1. In conclusion, TDN notably promoted tissue repair after urethral injury in rats by regulating the immune response, inhibiting fibrosis and enhancing cellular metabolism. These findings highlight TDN as a promising therapeutic candidate for urethral injury and offer novel insights into immune-regulatory strategies for the treatment of other fibrotic diseases.

*Correspondence to:* Dr Jian Li, Department of Sports Medicine, The Beijing Jishuitan Hospital Guizhou Hospital, 206 Sixian Street, Baiyun, Guiyang, Guizhou 550014, P.R. China
E-mail: 18213498761@163.com

*Contributed equally

*Key words:* urethral injury, fibrosis, immune response, tetrahedral DNA nanostructure, cell cycle regulation

## Introduction

Urethral injury is a common form of urinary tract trauma, often caused by external injury, surgical intervention or infection (1,2). This type of injury frequently leads to urethral stricture and fibrosis, resulting in severe functional impairment (1). Due to the complexity of tissue repair and lack of effective therapeutic options, urethral injury presents notable clinical challenges (3). Urethral injury not only affects physiological functions but also markedly compromises the quality of life of patients in the long term (4). Therefore, developing effective therapeutic approaches for urethral repair and inhibiting fibrosis remains an important clinical and research challenge (5).

The repair process following urethral injury involves complex biological responses, including immune regulation, cellular proliferation and migration and extracellular matrix deposition (5,6). The immune response and fibrosis progression serve notable roles in these processes (7,8). Activation of the immune system following urethral injury often triggers excessive inflammation, which subsequently leads to fibrosis (9). Fibrosis impairs the structural and functional integrity of the urethra, exacerbating urethral stricture and contributing to chronic urinary dysfunction. Thus, precise regulation of immune responses, cellular metabolism and proliferation is important for effective inhibition of fibrosis (10,11). Therefore, therapeutic strategies simultaneously modulating immune responses and preventing the progression of fibrosis are required.

Rapamycin, a commonly used immunosuppressant, is widely utilized in organ transplantation and immune-related diseases (12). Previously, considerable attention has been paid

to the potential therapeutic benefits of rapamycin in fibrotic conditions. Rapamycin primarily inhibits the mTOR signaling pathway, thereby modulating immune responses, regulating cell proliferation and effectively inhibiting fibrosis (13). Nonetheless, notable clinical limitations, including side effects and drug resistance, restrict the broader application of Rapamycin (14-16). Therefore, studies (17-19) have increasingly focused on alternative therapeutic agents or combination therapy, including DNA nanostructure-based immunomodulators and anti-fibrotic interventions targeting the TGF-β/Smad pathway, either alone or combined with immune regulatory strategies.

The present study focused on novel immunomodulatory molecules, tetrahedral DNA nanostructures (TDNs), self-assembled tetrahedral framework nucleic acids characterized by high structural stability, notable biocompatibility and efficient cellular uptake (20). Due to these unique properties, TDNs have attracted considerable attention in biomedical research (21,22). Previous studies have shown that TDN exhibits significant therapeutic effects in inflammatory diseases, cancer and fibrosis. Mechanistically, TDN regulates immune responses by modulating macrophage polarization and suppressing excessive inflammatory signaling (23,24), while also exerting anti-fibrotic effects by inhibiting fibroblast activation and reducing extracellular matrix deposition (25,26). However, the potential role of TDN and its underlying mechanisms in urethral injury repair remain to be fully elucidated. Therefore, the present study investigated the therapeutic efficacy of TDN in urethral injury and elucidated the underlying mechanisms. Specifically, the present study assessed the role of TDN in immune modulation, regulation of cellular metabolism and inhibition of fibrosis.

To investigate the therapeutic potential of TDN in urethral injury, the present study established a rat model of urethral injury via mechanical trauma (27). This model effectively mimicked the pathological conditions observed in clinical urethral injury, including localized inflammation and subsequent fibrosis, providing a robust experimental platform for assessing therapeutic efficacy (28). TDN was administered to rats with ureteral injury to observe its effects on immune responses, cell proliferation, fibrosis and tissue repair. Additionally, transcriptomic profiling and differential gene network analysis were conducted to unravel the molecular mechanisms through which TDN regulates the immune response, cell metabolism and fibrosis.

Overall, the novelty of the present study lies in the application of TDN in the treatment of urethral injury and the comprehensive assessment of the underlying mechanisms. Particularly, the present study examined the role of TDN in immune regulation and fibrosis inhibition.

## Materials and methods

*Animals and grouping*. The present study used 24 healthy male Sprague-Dawley rats (age, 6-8 weeks; body weight, 180-220 g at the start of the study), which were purchased from SPF Biotechnology Co., Ltd. [license no. SCXK (Beijing) 2019-0010]. The rats were housed under standard environmental conditions (temperature, 22±2˚C; humidity, 50±10%; 12-h light/dark cycle) with free access to food and water, and were acclimated for 1 week before the experiment. The rats were randomly divided into four groups: Control (n=6; intraperitoneal injection of an equal volume of saline every other day; injection volume, 0.2 ml per rat), model (n=6; urethral injury followed by intraperitoneal injection of saline every other day; injection volume, 0.2 ml per rat), model + rapamycin [n=6; 2.0 mg/kg of rapamycin (cat. no. HY-10219; MedChemExpress) injected intraperitoneally every other day after injury] and model + TDN (n=6; 10 nmol/day TDN administered via tail vein injection daily after injury; injection volume, 0.2 ml per rat). TDN was freshly prepared in TM buffer (10 mM Tris-HCl, 5 mM $MgCl_2$; pH 8.0), and its successful assembly and purity were confirmed. Animal experiments were approved by the Experimental Animal Welfare and Ethics Committee of Guizhou Medical University (approval no. 2502311; Guiyang, China).

*Preparation and verification of TDN*. The four single-stranded DNAs used for TDN assembly were chemically synthesized by Sangon Biotech Co., Ltd. TDN was synthesized by self-assembly of four single-stranded DNAs at a final concentration of 30 $\mu$M in TM buffer (10 mM Tris-HCl, 5 mM $MgCl_2$; pH 8.0; cat. no. T10420; Shanghai Shangbao Biotechnology Co., Ltd.), followed by denaturation at 95˚C for 10 min and rapid cooling to 4˚C. The sequences of the four single-stranded DNAs were as follows: S1, 5'-ATTTATCACCCGCCATAGTAGACGTATCAC CAGGCAGTTGAGACGAACATTCCTAAGTCTGAA-3'; S2, 5'-ATTTATCACCCGCCATAGTAGACGTATCACCAGGCA GTTGAGACGAACATTCCTAAGTCTGAA-3'; S3, 5'-ACT ACTATGGCGGGTGATAAAACGTGTAGCAAGCTGTAA TCGACGGGAAGAGCATGCCCATCC-3'; and S4, 5'-ACG GTATTGGACCCTCGCATGACTCAACTGCCTGGTGAT ACGAGGATGGGCATGCTCTTCCCG-3'. The successful formation of TDN was verified by 1% agarose gel electrophoresis (cat. no. A8201; Beijing Solarbio Science & Technology Co., Ltd.) using SerRed nucleic acid stain (cat. no. G3606; Wuhan Servicebio Technology Co., Ltd.), with staining performed at room temperature for 20 min, and by UV-visible spectrophotometry (NanoPhotometer® N50; Implen GmbH). A distinct absorption peak was observed at ~260 nm, with a concentration of 184.35 ng/$\mu$l, confirming successful tetrahedral assembly and high purity (Fig. S1).

*Urethral injury model*. The urethral injury model was established based on previous studies with slight modifications (27,29-31). Rats were anesthetized with 1% pentobarbital sodium (40 mg/kg; intraperitoneal; cat. no. P3761; MilliporeSigma) and then fixed on a surgical platform (RWD Life Science Co., Ltd.). The surrounding hair of the penis was shaved using an electric clipper (Flyco), and the surgical field was disinfected with iodine tincture (Wuhan Servicebio Technology Co., Ltd.). A longitudinal incision was made on the ventral side of the penis to expose the urethra. Mechanical injury was induced using an 18-G needle (BD Biosciences), forming an injury of ~5 mm in length. After inducing injury, the urethral sponge and skin were sutured (Fig. S2) using 6-0 absorbable sutures (Ethicon, Inc.; Johnson & Johnson). The wound was disinfected daily with povidone-iodine solution (Wuhan Servicebio Technology Co., Ltd.), and body weight and wound healing were monitored.

At the end of the experiment, all rats were euthanized by intraperitoneal injection of sodium pentobarbital at a dose of 100 mg/kg (cat. no. P3761; MilliporeSigma). Death was confirmed by the absence of thoracoabdominal movements, a lack of corneal reflex upon gentle touch and no withdrawal response to a firm toe pinch after loss of consciousness.

*Retrograde urethrography*. After successful anesthesia with 1% pentobarbital sodium (40 mg/kg, intraperitoneal), as aforementioned, rats were fixed on a digital fluoroscopic table (DRX-Ascend; Carestream Health, Inc.). Experimental staff wore protective clothing (Wuhan Servicebio Technology Co., Ltd.) and inserted a 24-G intravenous catheter (BD Biosciences) into the anterior urethra via the urethral opening (32). Using real-time X-ray monitoring, one hand stabilized the urethra and catheter, while the other hand slowly injected the iodinated contrast agent (iohexol; 300 mg iodine/ml; GE Healthcare) into the bladder via the catheter. X-ray images were obtained to assess the narrowing of the urethral lumen.

*Hematoxylin and eosin (H&E) staining*. The urethral tissue was fixed in 4% paraformaldehyde solution [cat. no. NH250218; Nuohai Life Science (Shanghai) Co., Ltd.] at room temperature for 24-48 h. Following fixation, the tissues were rinsed with PBS (cat. no. G1101; Wuhan Servicebio Technology Co., Ltd.), dehydrated through a graded ethanol series [70, 80, 95% and absolute ethanol (CAS no. 64-17-5; analytical grade;; Chengdu Kelong Chemical Co., Ltd.)], and cleared with xylene (cat. no. 33535; Xilong Scientific Co., Ltd.). Samples were subsequently embedded in paraffin (Shanghai Huayong Paraffin Co., Ltd.) and sectioned at a thickness of 5 $\mu$m using a rotary microtome [HistoCore MULTICUT; cat. no. 149MULTIGC1; Leica Biosystems Co., Ltd.].

For H&E staining, paraffin-embedded sections were deparaffinized with xylene and rehydrated through descending concentrations of ethanol, followed by staining with hematoxylin solution (cat. no. G1004-100ML; Wuhan Servicebio Technology Co., Ltd.) at room temperature for 5 min, rinsed with running water, and counterstained with eosin staining solution (cat. no. G1108; Beijing Solarbio Science & Technology Co., Ltd.) at room temperature for 1-2 min. After dehydration and clearing with xylene, the sections were mounted using neutral resin mounting medium (cat. no. WG10004160; Wuhan Servicebio Technology Co., Ltd.) and histological images were captured using an inverted light microscope (TS2; Nikon Corporation).

*Histological staining*. Masson's trichrome staining was conducted to evaluate collagen deposition in the urethral tissue (33). The urethral tissue was fixed in 4% paraformaldehyde solution (cat. no. G1101; Wuhan Servicebio Technology Co., Ltd.) at room temperature for 24 h, dehydrated and embedded in paraffin. Sections with a thickness of 4 $\mu$m were prepared using a rotary microtome. Masson's trichrome staining was conducted at room temperature using a commercial kit (cat. no. G1006; Wuhan Servicebio Technology Co., Ltd.) according to the manufacturer's protocol, with the staining duration following the standard instructions. Images were captured at a magnification of x200 using a light microscope. Collagen fibers were stained blue, whereas muscle fibers, fibrin and red blood cells appeared red.

Immunohistochemical staining (34) was conducted to evaluate the expression of fibrosis markers, including α-smooth muscle actin (α-SMA; cat. no. AF1032; Affinity Biosciences), TGF-β1 (1:5,000; cat. no. 21898-1-AP; Proteintech Group, Inc.), collagen I (cat. no. AF7001; Affinity Biosciences), collagen III (1:1,000; cat. no. AF5457; Affinity Biosciences) and Smad3 (cat. no. 87035-1-RR; Proteintech Group, Inc.). Briefly, paraffin-embedded tissue sections prepared as aforementioned were sectioned at a thickness of 4 $\mu$m. Sections were then deparaffinized, rehydrated through a descending ethanol series and subjected to heat-induced antigen retrieval using citrate buffer (pH 6.0; cat. no. G1202; Wuhan Servicebio Technology Co., Ltd.). Subsequently, the sections were incubated with 3% hydrogen peroxide (Wuhan Servicebio Technology Co., Ltd.) to quench endogenous peroxidase activity and were blocked with 5% BSA (cat. no. CR2302110; Beijing Solarbio Science & Technology Co., Ltd.) for 30 min at room temperature; after which, the sections were incubated overnight at 4˚C with the corresponding primary antibodies diluted in 2% BSA at a dilution of 1:100. This was followed by incubation with a HRP-conjugated secondary antibody (cat. no. G1215; Wuhan Servicebio Technology Co., Ltd.) for 50 min at 37˚C. Color development was achieved using a DAB chromogenic kit (cat. no. G1211; Wuhan Servicebio Technology Co., Ltd.), and cell nuclei were counterstained with hematoxylin (cat. no. G1040-500ML; Wuhan Servicebio Technology Co., Ltd.) at room temperature for 2 min. Images were captured at a magnification of x200 using a light microscope (CX23; Olympus Corporation). Image-Pro Plus software (version 6.0; Media Cybernetics, Inc.) was employed to quantify the percentage and intensity of positive staining to assess the degree of fibrosis.

*Western blotting*. To evaluate the protein expression levels of α-SMA, TGF-β1, collagen I, Smad3 and collagen III, total protein was extracted from rat urethral tissues using RIPA lysis buffer (cat. no. G2002; Wuhan Servicebio Technology Co., Ltd.) containing protease and phosphatase inhibitor cocktail (cat. no. G2007; Wuhan Servicebio Technology Co., Ltd.). The protein concentration was determined using a BCA assay kit (cat. no. G2026; Wuhan Servicebio Technology Co., Ltd.) (35). Proteins (30 $\mu$g per lane) were separated using SDS-PAGE (10% gel; cat. no. P0012A; Beyotime Biotechnology) and transferred onto PVDF membranes (cat. no. IPVH00010; MilliporeSigma) using the wet transfer method. The membranes were blocked with 5% BSA for 1 h at room temperature, and incubated overnight at 4˚C with the following primary antibodies: α-SMA (1:1,000; cat. no. AF1032; Affinity Biosciences), TGF-β1 (1:5,000; cat. no. 21898-1-AP; Proteintech Group, Inc.), collagen I (1:1,000; cat. no. AF7001; Affinity Biosciences), collagen III (1:1,000; cat. no. AF5457; Affinity Biosciences) and Smad3 (1:10,000; cat. no. 66516-1-Ig; Proteintech Group, Inc.), and β-actin (1:25,000; cat. no. 66009-1-Ig; Proteintech Group, Inc.), which was used as a loading control.

After washing three times with TBS containing 0.1% Tween-20 (cat. no. G0004-500M; Wuhan Servicebio Technology Co., Ltd.), the membranes were incubated for 1 h at 37˚C with HRP-conjugated goat anti-rabbit IgG secondary antibody (1:3,000; cat. no. GB23303; Wuhan Servicebio Technology Co., Ltd.) or HRP-conjugated goat anti-mouse

IgG secondary antibody (1:5,000; cat. no. GB23301; Wuhan Servicebio Technology Co., Ltd.), as appropriate. Protein bands were visualized using an enhanced chemiluminescence kit (cat. no. G2014; Wuhan Servicebio Technology Co., Ltd.) and images were captured with a ChemiDoc™ MP Imaging System (cat. no. 12003154; Bio-Rad Laboratories, Inc.). Band intensities were semi-quantified using Image-Pro Plus software (version 6.0).

*Transcriptome sequencing and analysis*. To explore the molecular mechanisms underlying urethral injury and repair, total RNA was extracted from rat urethral tissues using TRIzol® reagent (cat. no. 15596026; Invitrogen; Thermo Fisher Scientific, Inc.) according to the manufacturer's protocol.

The RNA concentration and purity were assessed using a NanoDrop™ 2000 spectrophotometer (cat. no. ND-2000; Thermo Fisher Scientific, Inc.), and RNA integrity was verified by 1% agarose gel electrophoresis (cat. no. A8201; Beijing Solarbio Science & Technology Co., Ltd.). High-throughput sequencing libraries were prepared using the NEBNext® Ultra™ RNA Library Prep Kit for Illumina (cat. no. E7530L; New England BioLabs, Inc.) and sequencing was performed on an Illumina NovaSeq 6000 platform using the NovaSeq 6000 S4 Reagent Kit v1.5 (300 cycles; cat. no. 20028312; Illumina, Inc.) (36). Paired-end RNA sequencing (2x150 bp) was performed in a forward-reverse orientation, with the final libraries loaded at a concentration of 300 pM. The quality of raw sequencing data was evaluated using FastQC (version 0.11.9; Babraham Bioinformatics), and adaptor trimming and filtering were conducted using Trimmomatic (version 0.39; http://www.usadellab.org/cms/?page=trimmomatic). Clean reads were aligned to the rat reference genome (Rnor_6.0) using HISAT2 (version 2.2.1; https://daehwankimlab.github.io/hisat2/). Principal component analysis (PCA) was performed to evaluate global transcriptional differences among samples and to assess the consistency of biological replicates. Sample-to-sample correlation analysis was performed using Pearson correlation coefficients based on normalized gene expression values to examine intra-group repeatability and inter-group variability. The results were visualized using PCA for dimensionality reduction and correlation heatmaps generated using the pheatmap package (version 1.0.12; https://cran.r-project.org/package=pheatmap) in R software (version 4.2.2; The R Foundation for Statistical Computing; https://www.r-project.org/). Differential gene expression analysis was performed using the DESeq2 package (version 1.38.0; https://bioconductor.org/packages/DESeq2/) in R software, with thresholds of $|\log2(\text{fold change})| \geq 0.5$ and $P<0.05$ to identify significantly differentially expressed genes (DEGs). Functional enrichment analyses were conducted using the Kyoto Encyclopedia of Genes and Genomes (KEGG) database (https://www.kegg.jp) to identify pathways related to fibrosis, inflammation, immune regulation, metabolism, cell cycle regulation and tissue repair. Specifically, pathways were selected based on their direct relevance to immune regulation, inflammation, metabolism, cell cycle regulation and tissue repair, which are key processes associated with urethral injury and TDN-mediated therapeutic effects. Disease-related pathways with limited mechanistic relevance to urethral pathology were excluded from the final analysis. Statistical analyses and visualization were conducted in R software using the pheatmap package and ggplot2 package (version 3.4.0; https://cran.r-project.org/package=ggplot2) to display gene expression patterns and enrichment results.

*Reverse transcription-quantitative PCR (RT-qPCR)*. To validate the transcriptome sequencing results, total RNA was extracted from rat urethral tissues using TRIzol® reagent (cat. no. 15596026; Invitrogen; Thermo Fisher Scientific, Inc.) according to the manufacturer's instructions. Reverse transcription was performed using the PrimeScript™ RT reagent kit with gDNA eraser (cat. no. RR047A; Takara Bio, Inc.) to synthesize cDNA. Reverse transcription was performed at 42˚C for 15 min, followed by enzyme inactivation at 85˚C for 5 sec. qPCR was conducted using TB Green® Premix Ex Taq™ II (cat. no. RR820A; Takara Bio, Inc.) on a QuantStudio™ 5 Real-Time PCR System (cat. no. A28574; Applied Biosystems; Thermo Fisher Scientific, Inc.). Each reaction (20 $\mu$l) contained 10 $\mu$l SYBR Green mix, 1 $\mu$l cDNA template, 0.4 $\mu$l of each primer (10 $\mu$M) and 8.2 $\mu$l nuclease-free water. The PCR amplification conditions were as follows: 95˚C for 30 sec, followed by 40 cycles of 95˚C for 5 sec and 60˚C for 30 sec. The expression levels of the cell cycle-related genes cyclin B1 (*Ccnb1*), ribonucleotide reductase regulatory subunit M2 (*Rrm2*), polo-like kinase 1 (*Plk1*) and cyclin-dependent kinase 1 (*Cdk1*), as well as the inflammatory cytokines *IL-6*, *IL-1β* and *TNF-α*, were analyzed, with *GAPDH* used as the internal control. The relative gene expression levels were calculated using the $2^{-\Delta\Delta Cq}$ method for quantification, as previously described by Livak and Schmittgen (37). Primer sequences are listed in Table SI.

*Differential gene network analysis*. After identifying DEGs from the transcriptome data, protein-protein interaction (PPI) network analysis was performed using the Search Tool for the Retrieval of Interacting Genes/Proteins database (version 12.0; https://string-db.org/) to evaluate gene-gene associations. A confidence score threshold of 0.7 (high confidence) was applied to filter significant interactions and the resulting interaction data were imported into Cytoscape software (version 3.10.0; Cytoscape Consortium) for visualization. The PPI network was optimized using the cytoHubba plug-in (version 0.1; https://apps.cytoscape.org/apps/cytohubba) to identify hub genes with the highest degree of connectivity.

These key genes were analyzed in the context of fibrosis, extracellular matrix remodeling and cell cycle regulation to explore their biological significance and potential roles in the pathogenesis of urethral injury.

*ELISA*. The serum concentrations of IL-6, IL-1β and TNF-α were measured using ELISA kits: IL-6 (cat. no. SEA079Ra; CLOUD-CLONE CORP), IL-1β (cat. no. SEA563Ra; CLOUD-CLONE CORP) and TNF-α (cat. no. SEA133Ra; CLOUD-CLONE CORP). The assays were conducted according to the manufacturer's protocols. Absorbance was read at 450 nm using a SpectraMax® iD3 microplate reader (iD3; Molecular Devices, LLC). Cytokine levels were quantified based on standard curves and expressed as pg/ml. These data were used to evaluate the systemic immune and inflammatory responses following urethral injury.

*Single-sample gene set enrichment analysis (ssGSEA).* ssGSEA was performed to evaluate the immune microenvironment and quantify immune cell infiltration in rat urethral tissues.

The analysis was based on the normalized transcriptome expression matrix. The GSVA package (version 1.46.0; https://bioconductor.org/packages/GSVA/) in R software was used to calculate the enrichment scores of immune-related gene sets for each sample. Immune cell-related gene sets representing 24 immune cell types were derived directly from the immune cell signature gene sets defined in a previous study by Bindea *et al* (38) and were curated for application in ssGSEA. These gene sets included signatures for macrophages, T cells, natural killer cells, dendritic cells and neutrophils. The enrichment scores were visualized using the ggplot2 package and the pheatmap package n R., enabling quantitative assessment of immune cell infiltration and characterization of immune landscape alterations associated with urethral injury and TDN treatment.

*Fibroblast isolation and culture.* Primary fibroblasts were isolated from rat urethral tissues under sterile conditions. Briefly, freshly harvested urethral tissues were rinsed 3-5 times with PBS supplemented with 5% penicillin-streptomycin solution (Dalian Meilun Biology Technology Co., Ltd.), with each wash lasting 5 min. The tissues were then minced into small fragments using sterile scissors and digested with 0.25% trypsin (Dalian Meilun Biology Technology Co., Ltd.) at 37˚C in a humidified incubator with 5% $CO_2$ for 60 min.

Following enzymatic digestion, 6 ml complete Dulbecco's modified Eagle's medium (DMEM; Dalian Meilun Biology Technology Co., Ltd.) supplemented with 10% fetal bovine serum (FBS; Gibco; Thermo Fisher Scientific, Inc.) and 1% penicillin-streptomycin was added to terminate digestion. The cell suspension was collected and centrifuged at 1,000 rpm for 5 min. The resulting cell pellet was resuspended in complete DMEM and transferred to culture flasks for incubation at 37˚C in a humidified atmosphere containing 5% $CO_2$.

The culture medium was replaced every 2-3 days. When cells reached ~80% confluence, fibroblasts were passaged using 0.25% trypsin digestion. Cells were washed twice with PBS, digested until most cells became rounded and detached, and digestion was terminated with complete DMEM. After centrifugation at ~200 x g for 5 min at room temperature, the cells were resuspended in fresh complete medium and passaged at a ratio of 1:2. Primary rat urethral fibroblasts were cultured in complete DMEM supplemented with 10% FBS and 1% penicillin-streptomycin at 37˚C in a humidified incubator containing 5% $CO_2$. When cells reached 70-80% confluence, *in vitro* treatments were performed. Cells were divided into the following three groups: Control, TGF-β-treated and TGF-β + TDN-treated groups. For induction of vimentin expression, fibroblasts were treated with TGF-β (5 ng/ml; cat. no. 80116-R08H; Beijing Sino Technology Co., Ltd.) for 24 h. For the intervention group, TDN (1 $\mu$M) was added simultaneously with TGF-β, and the cells were co-treated for 24 h at 37˚C. After treatment, the cells were collected for immunohistochemical analysis of vimentin expression, as described in the Materials and methods section.

*Immunocytochemical staining for vimentin.* To evaluate vimentin expression in fibroblasts, immunocytochemical staining was performed. After treatment, the cells were washed with PBS and fixed with 4% paraformaldehyde at room temperature overnight. Following fixation, the cells were washed with PBS, subjected to antigen retrieval using pepsin solution at 37˚C for 30 min, and endogenous peroxidase activity was quenched with 3% hydrogen peroxide for 20 min at room temperature. The cells were then blocked with 5% bovine serum albumin (cat. no. CR2302110; Beijing Solarbio Science & Technology Co., Ltd.) for 30 min at 37˚C and incubated overnight at 4˚C with a primary antibody against vimentin (1:150; cat. no. AFRM0062; Hunan Aifang Biotechnology Co., Ltd.), diluted in 2% bovine serum albumin. After washing, the cells were incubated with a polymer-based secondary antibody using a universal two-step detection kit (cat. no. PV-9000; OriGene Technologies, Inc.) according to the manufacturer's instructions. Color development was achieved using a DAB chromogenic kit, and cell nuclei were counterstained with hematoxylin for 5 min at room temperature. Representative images were captured using a light microscope, and quantitative analysis was performed using Image-Pro Plus software, as aforementioned.

*H&E staining of fibroblasts.* Primary rat urethral fibroblasts were isolated from urethral tissues and cultured under standard conditions as aforementioned. After expansion, fibroblasts were enzymatically dissociated and seeded onto glass coverslips for cell attachment. Following culture, fibroblast samples (n=6) were provided for histological evaluation, including H&E staining and immunocytochemical staining. H&E staining was performed as aforementioned to assess fibroblast morphology, and representative images were acquired using a light microscope.

*Immunofluorescence identification of fibroblasts.* To confirm the purity and identity of the fibroblasts isolated from rat urethral tissues, immunofluorescence staining for α-SMA and CD90 was performed. Cells were fixed with 4% paraformaldehyde (cat. no. G1101; Wuhan Servicebio Technology Co., Ltd.) for 15 min at room temperature, permeabilized with 0.3% Triton X-100 (cat. no. G1203; Wuhan Servicebio Technology Co., Ltd.) and blocked with 5% BSA for 30 min at room temperature. The cells were incubated with primary antibodies against α-SMA (1:100; cat. no. AF1032; Affinity Biosciences) and CD90 (1:100; cat. no. DF4804; Affinity Biosciences) overnight at 4˚C. After washing with PBS, cells were incubated with goat anti-rabbit IgG H&L (Alexa Fluor™ 488-conjugated; 1:200; cat. no. ab150077; Abcam) secondary antibodies for 40 min at 37˚C. Nuclei were counterstained with DAPI (cat. no. G1012; Wuhan Servicebio Technology Co., Ltd.) at room temperature for 8 min in the dark. Fluorescence images were captured using a Nikon TS2-S-SM inverted fluorescence microscope (Nikon Corporation). The results showed negative α-SMA staining together with positive CD90 expression, indicating that the isolated cells were predominantly fibroblasts and excluding myofibroblast contamination.

*Statistical analysis.* All quantitative data are presented as the mean ± standard deviation from at least three independent

experiments. Statistical analyses were performed using GraphPad Prism software (version 9.0; Dotmatics). This approach was used for multi-group quantitative analyses presented in the figures. Comparisons among three or more groups were performed using one-way analysis of variance followed by Tukey's post hoc test. $P<0.05$ was considered to indicate a statistically significant difference. Transcriptome data were analyzed using R software. The ggplot2 (version 3.4.0), pheatmap (version 1.0.12) and ClusterProfiler (version 4.6.0; https://bioconductor.org/packages/clusterProfiler/) packages were used for data visualization and functional enrichment analysis. Sample correlation analysis was performed using Pearson correlation analysis based on normalized gene expression levels, and the results are presented as a sample-to-sample correlation heatmap. All figures were generated using GraphPad Prism and R and assembled in Adobe Illustrator (version 2023; Adobe Systems, Inc.) for final presentation.

## Results

*Validation of the rat model of urethral injury.* To ensure reliability, the urethral injury model was validated from multiple aspects. Fig. 1A shows the tissue collection images of rat urethras in different groups. Postoperative body weight recordings showed that the control group gradually gained weight, whereas the model group experienced marked weight loss. Notably, body weight in the rapamycin and TDN groups exhibited a slight, non-significant decrease and remained relatively stable overall (Fig. 1B). Urethrography showed that the urethras of rats were healthy in the control group, while urethral stenosis was successfully developed in the model group. Urethral stenosis improved after treatment with rapamycin and TDN (Fig. 1C). H&E staining showed that in the model group, the mucosal layer of the urethra was notably thickened and the lumen was narrower, with marked inflammatory cell infiltration compared with the control group. Consistent with the results of urethrography, the rapamycin and TDN groups showed notable improvements in urethral histological structure, with reduced luminal narrowing and improved tissue organization, suggesting an attenuation of urethral injury following rapamycin and TDN treatment (Fig. 1D).

These results suggested that the urethral injury model was successfully established, and different treatment groups exhibited notable differences in terms of urethral damage and fibrosis. Particularly, the results supported the therapeutic effects of Rapamycin and TDN, further supporting their efficacy in alleviating urethral injury.

*Differential gene expression induced by urethral injury in rats.* Transcriptome sequencing revealed the relationship between different treatments and gene expression. PCA (Fig. 2A) showed that samples from the same group clustered closely together, whereas samples from different groups were clearly separated, indicating distinct transcriptomic profiles among the control model, and treatment groups. Consistently, sample correlation analysis (Fig. 2B) revealed high correlation coefficients among biological replicates within each group and lower correlations between different groups, demonstrating good intra-group reproducibility and clear inter-group differentiation. Differential expression analysis identified 3,008 DEGs, including 1,248 upregulated and 819 downregulated genes between the model and control groups, 194 upregulated and 45 downregulated genes between the Rapamycin and model groups, and 206 upregulated and 496 downregulated genes between the TDN and model groups (Fig. 2C and D). All three comparisons shared 41 genes (Fig. 2E). The slight discrepancy in gene numbers between the Venn diagram (Fig. 2E) and the DEG counts shown in Fig. 2C and D is due to differences in gene inclusion criteria, as one gene located at the significance threshold was included in the Venn analysis but excluded from the final DEG count. These genes, including genes related to metabolism, keratin, acute-phase response, inflammation and immune function, exhibited differential expression patterns after different treatments (Fig. 2F).

KEGG pathway enrichment analysis of all differential genes revealed that differential genes between the model and control groups were predominantly enriched in: i) Immune-related and inflammation-related pathways, including 'Cytokine-cytokine receptor interaction', 'Chemokine signaling pathway', 'NOD-like receptor signaling pathway' and 'TNF signaling pathway'; ii) survival, proliferation and metabolism-related pathways, such as 'PI3K-Akt signaling pathway', 'MAPK signaling pathway', 'cAMP signaling pathway' and 'FoxO signaling pathway'; and iii) cardiovascular and metabolic pathways, including the 'Lipid and atherosclerosis' and 'Oxidative phosphorylation' pathways. Differential genes between the Rapamycin and model groups were mainly enriched in: i) Immune-related and inflammation-related pathways, such as 'Cytokine-cytokine receptor interaction', 'Chemokine signaling pathway', 'Toll-like receptor signaling pathway', 'NF-κB signaling pathway', 'TNF signaling pathway' and 'IL-17 signaling pathway'; and ii) antigen presentation and immune recognition pathways, including the 'Antigen processing and presentation' and 'Phagosome' pathways. Differential genes between the TDN and model groups were predominantly enriched in: i) Immune-related and inflammation-related pathways, such as 'Cytokine-cytokine receptor interaction', 'NF-κB signaling pathway' and 'NOD-like receptor signaling pathway'; ii) metabolism-related and cell function-related pathways, such as the 'Nucleotide metabolism', 'Glutathione metabolism' and 'Glycine, serine and threonine metabolism' pathways; and iii) cell cycle-related pathways such as the 'p53 signaling pathway' (Fig. 2G).

*Urethral fibrosis induced by urethral injury in rats.* Masson's trichrome staining showed a notable increase in collagen fibers in the urethral tissue of the model group compared with the control group. By contrast, the content of collagen fibers decreased after treatment with rapamycin and TDN. Immunohistochemical staining also demonstrated upregulated expression of fibrosis markers, such as α-SMA, TGF-β1, collagen I, collagen III and Smad3, in the model group compared with the control group, but their expression was subsequently decreased in the rapamycin and TDN groups compared with that in the model group (Fig. 3A).

Quantitative analysis of Masson's trichrome-stained sections using Image-Pro Plus software revealed a significant increase in collagen fiber content in the model group compared with that in the control group ($P<0.001$), along with a significant increase in the expression of fibrosis markers based on

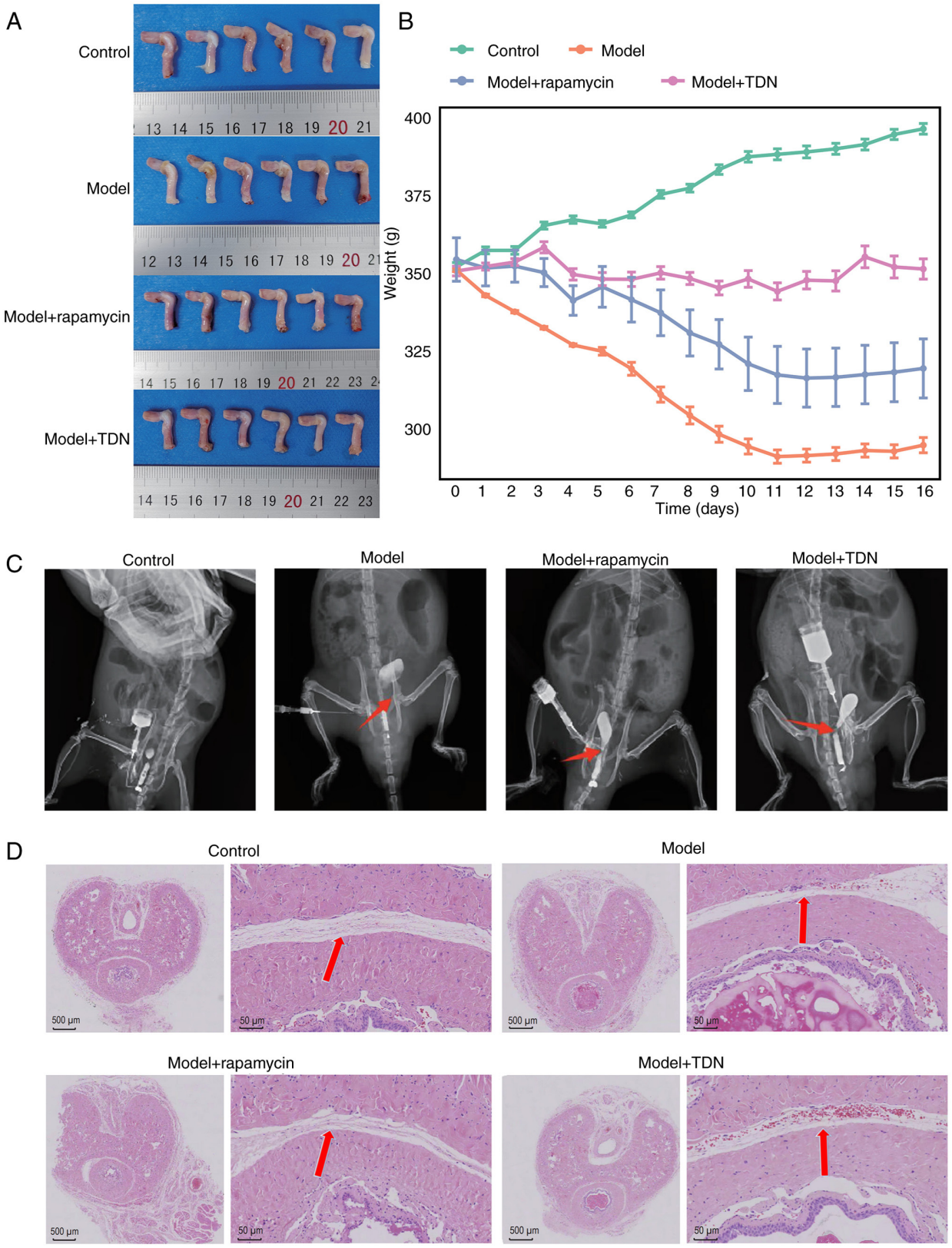


Figure 1. (A) Urethral tissue collection images from the control, model, model + rapamycin, and model + TDN group. (B) Body weight monitoring curves for rats in all groups over time. (C) Urethrographic imaging results for each group, with red arrows indicating the location of urethral injury model establishment. (D) Hematoxylin and eosin staining results for urethral tissues from each group. Red arrows indicate urethral lumen narrowing and associated fibrotic changes in the injured urethra. Scale bar, 500 $\mu$m (left) and 50 $\mu$m (right). TDN, tetrahedral DNA nanostructure.

immunohistochemical analyses (P<0.01 or P<0.001). By contrast, the rapamycin and TDN groups exhibited a significant decrease in collagen content and reduced expression of fibrosis markers compared with the model group (P<0.05, P<0.01 or P<0.001), suggesting that rapamycin and TDN treatment exerted inhibitory effects on fibrosis (Fig. 3B).

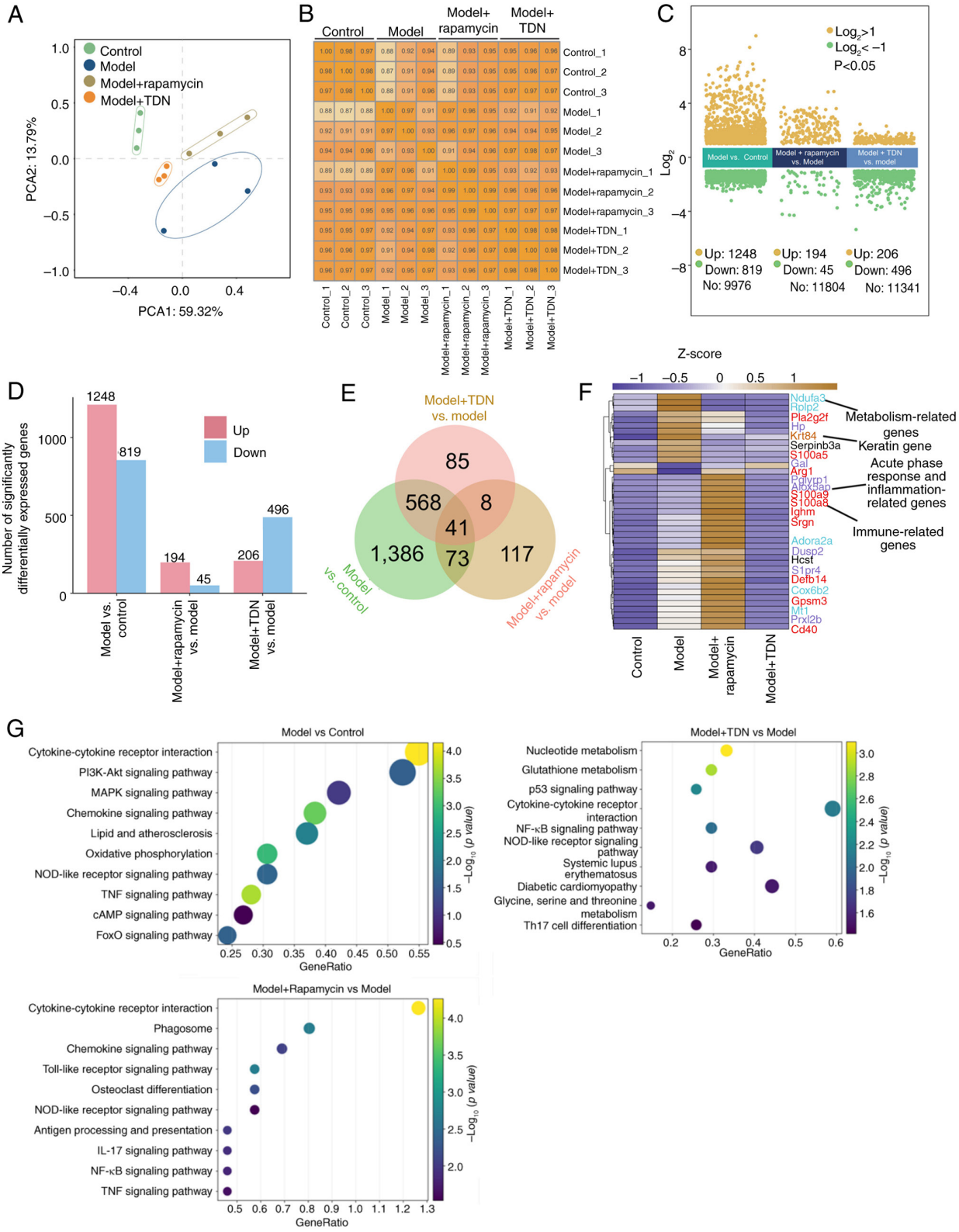


Figure 2. (A) PCA results. Different colors represent different treatment groups. (B) Sample correlation heatmap. The color intensity corresponds to correlation values. (C) Combined volcano plot showing the distribution of FCs in differentially expressed genes in the three group comparisons (model vs. control; model + rapamycin vs. model; model + TDN vs. model), with yellow dots representing upregulated genes and green dots representing downregulated genes. (D) Bar chart of differential gene counts showing the number of differential genes in the three group comparisons. (E) Venn diagram of differential genes displaying the distribution of differential genes in the three group comparisons. The numbers in different areas represent specific intersections or unique differential genes. (F) Heatmap showing the expression patterns of 25 common differentially expressed genes identified from three pairwise comparisons, displayed across four experimental groups (Control, Model, Model + rapamycin, and Model + TDN). Each row represents one gene and each column represents an individual sample. Color gradients indicate normalized gene expression levels. (G) KEGG pathway enrichment analysis of differentially expressed genes from the three pairwise comparisons (model vs. control; model + rapamycin vs. model; model + TDN vs. model). Enrichment results are presented as dot plots. The x-axis represents the GeneRatio, and the size of each dot reflects the proportion of genes enriched in the corresponding pathway. Dot color indicates the statistical significance expressed as -log10(P-value). KEGG pathways are displayed consistently across the three comparisons to facilitate direct visual comparison. KEGG, Kyoto Encyclopedia of Genes and Genomes; TDN, tetrahedral DNA nanostructure; FC, fold change; PCA, principal component analysis.

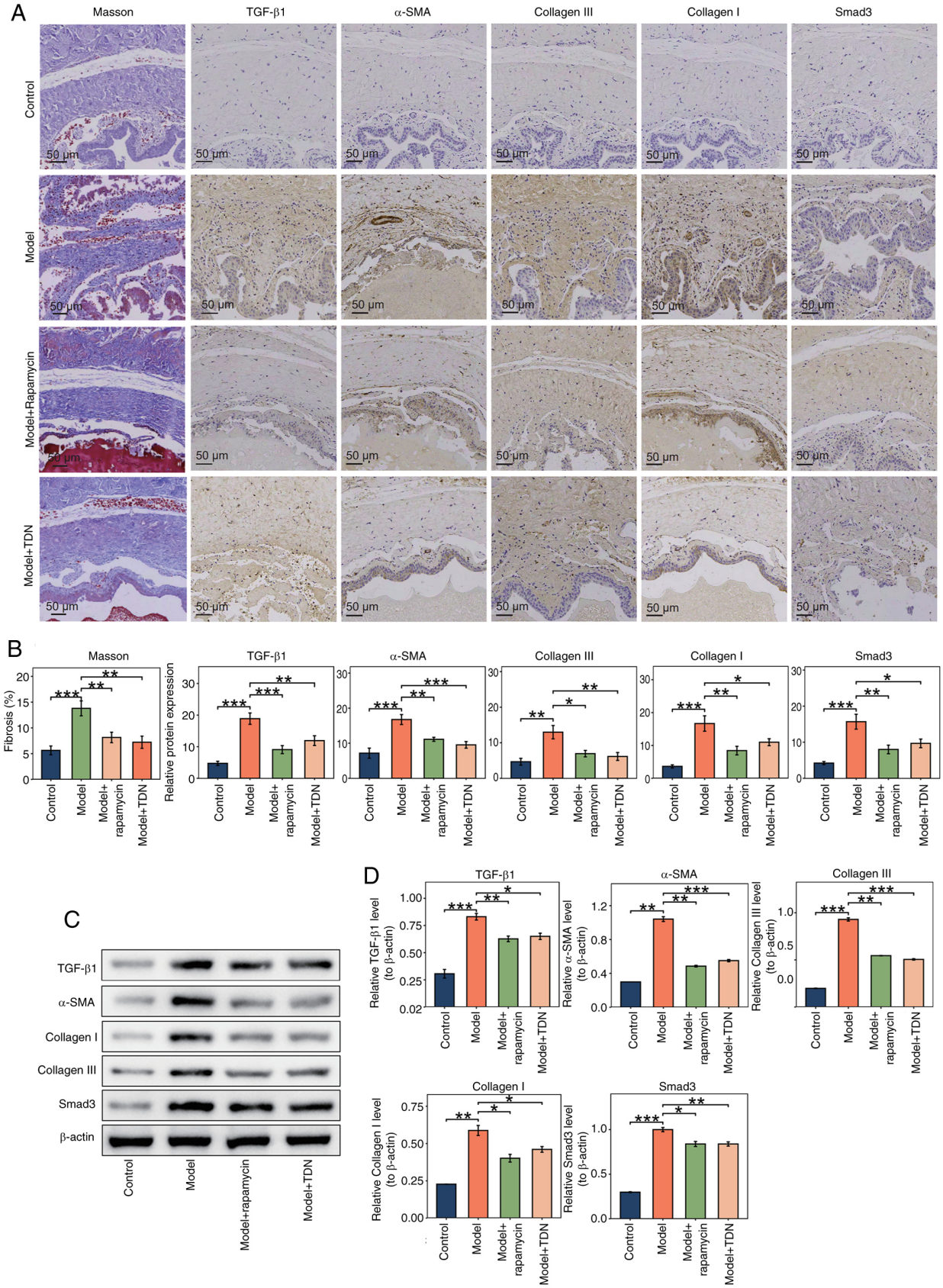


Figure 3. (A) Masson's trichrome staining and immunohistochemistry results. Masson's trichrome staining detected changes in collagen fibers in urethral tissues, with collagen fibers appearing blue and muscle fibers, fibrin and red blood cells appearing red. Immunohistochemistry staining showed the cell nuclei in blue and positive protein staining for the fibrosis markers α-SMA, TGF-β1, collagen I, collagen III and Smad3 in brown. Images are presented at a magnification of x200. (B) Statistical analysis of Masson's trichrome staining and immunohistochemistry results. Staining results were analyzed with Image-Pro Plus software(version 6.0; Media Cybernetics, Inc.), followed by bar chart construction using GraphPad Prism. $^{*}$P<0.05, $^{**}$P<0.01 and $^{***}$P<0.001. (C) Western blot analysis results. Western blot analysis was used to detect the protein expression of fibrosis markers in urethral tissue. (D) Statistical analysis of western blotting results. Band densities were analyzed using Image-Pro Plus software(version 6.0; Media Cybernetics, Inc.), and bar charts were drawn with GraphPad Prism. $^{*}$P<0.05, $^{**}$P<0.01 and $^{***}$P<0.001. α-SMA, α-smooth muscle actin; TDN, tetrahedral DNA nanostructure.

Western blot analysis supported these findings, with significant increases observed in the protein expression levels of α-SMA, TGF-β1, collagen I, Smad3 and collagen III in the model group compared with the control group (P<0.01 or P<0.001). Compared with the model group, significant decreases in the expression of these markers were observed in the Rapamycin and TDN groups (P<0.05, P<0.01 or P<0.001) (Fig. 3C and D).

Overall, TDN effectively mitigated the progression of urethral fibrosis in the rat model by downregulating the expression levels of the fibrosis markers α-SMA, TGF-β1, collagen I, collagen III and Smad3, as well as by inhibiting collagen deposition as evidenced by Masson's trichrome staining Masson's trichrome staining and immunohistochemical staining indicated that TDN significantly suppressed the accumulation of collagen fibers and downregulated fibrosis markers in the model group, suggesting that TDN displayed protective effects against fibrosis. These results provide a theoretical basis for exploring the potential application of TDN.

*Immune response induced by urethral injury in rats.* Immune infiltration scores in rats were analyzed by ssGSEA to unravel the relationship between urethral injury and the immune system. The model group showed marked immune cell infiltration of innate and adaptive immune cells, particularly macrophages, monocytes, and activated $CD4^+$ and $CD8^+$ T cells, whereas neutrophil infiltration was reduced in the model group compared with in the control group, indicating that urethral injury induced a shift from acute neutrophil-dominated inflammation toward a macrophage- and lymphocyte-driven immune response, suggesting the development of a sustained inflammatory and immune remodeling process (Fig. 4A). Furthermore, the immune infiltration score heatmap showed marked differences in immune cell infiltration across the groups, with TDN treatment markedly reducing immune cell infiltration compared with that in the model group (Fig. 4B).

RT-qPCR showed that the mRNA expression levels of the inflammatory cytokines IL-6, IL-1β and TNF-α were significantly increased in the model group compared with the control group (P<0.001). Compared with those in the model group, rapamycin and TDN significantly downregulated the levels of these inflammatory cytokines (P<0.01 or P<0.001), indicating that after urethral injury, both rapamycin and TDN can modulate the immune response at the transcriptional level (Fig. 4C). An ELISA also supported these findings. The serum levels of inflammatory cytokines were significantly higher in the model group compared with the control group (P<0.001). Compared with those in the model group, the serum levels of inflammatory cytokines were significantly decreased in the treatment groups (P<0.01 or P<0.001) (Fig. 4D).

These results suggested that urethral injury significantly enhanced the immune response, while TDN effectively inhibited immune cell infiltration and lowered the expression levels of inflammatory cytokines, reducing the immune response triggered by urethral injury. TDN modulated the immune response at the transcriptional level and prevented the release of inflammatory cytokines, indicating its potential anti-inflammatory and immunoregulatory properties after urethral injury.

*Expression levels of Ccnb1, Rrm2, Plk1 and Cdk1 in urethral injury.* Transcriptomic analysis revealed that the expression levels of cell cycle-related genes, such as *Ccnb1*, *Rrm2*, *Plk1* and *Cdk1*, were notably upregulated in the model group compared with the control group, suggesting that urethral injury may have accelerated cell proliferation by promoting cell cycle progression Compared with those in the model group, the expression levels of most of these genes were decreased in the rapamycin and TDN groups, whereas Rrm2 showed no marked reduction in the rapamycin group, indicating that rapamycin and TDN may have regulated cell proliferation by inhibiting the expression of cell cycle-related genes. Heatmap and boxplot analyses (Fig. 5A and B) visualized between-group differences in the expression of these genes, showing that after urethral injury, the expression of cell cycle-related genes was effectively controlled in the intervention groups.

RT-qPCR further supported the results of the transcriptomic analysis. The analysis (Fig. 5C) showed that, compared with those in the control group, the mRNA expression levels of *Ccnb1*, *Rrm2*, *Plk1* and *Cdk1* were significantly enhanced in the model group (P<0.05 or P<0.001). Furthermore, the expression levels of cell cycle genes were significantly lower in the rapamycin and TDN groups compared with the model group (P<0.05 or P<0.001), providing evidence that rapamycin and TDN regulated the expression of genes related to the cell cycle to inhibit cell proliferation.

*Differential gene network analysis.* Differential gene network analysis revealed the relationships between genes in the rat model of urethral injury. The network illustrated genes with significant interactions after urethral injury, with gene nodes connected by edges. The density of the network reflected the strength of gene interactions. By analyzing the interaction networks of these genes, the present study divided them into several functional modules, each representing a specific biological characteristic or function (Fig. 6).

*Energy metabolism and cell function.* This module contained genes related to cell energy metabolism, such as phosphoglycerate kinase 1 *(Pgk1)* and lactate dehydrogenase A *(Ldha),* indicating that urethral injury reprogrammed cell metabolism to support the repair and recovery of damaged cells. The changes in genes in this module suggested that cell energy metabolism may have served a key role after injury, providing sufficient energy for the repair process.

*Tissue repair and fibrosis.* Changes in the expression of genes related to tissue repair and fibrosis, such as biglycan (*Bgn*) and matrix metallopeptidase 3 (*Mmp3*), revealed that urethral injury may have triggered a fibrotic response, changing the tissue structure. The initiation of fibrosis may have affected normal urethral function, with gene regulatory changes indicating that the repair process after injury may have been accompanied by unwanted fibrotic reactions.

*Immune response.* This module involved immune-related genes, such as *IL-1β* complement C1q A chain (*C1qa*) and complement C1q B chain (*C1qb*), whose expression was significantly upregulated after urethral injury. Activation of these immune genes supported the important role of the immune system in the repair process after injury.

*Cell proliferation and migration.* Genes related to cell proliferation and migration, such as Cd68 and actin γ1

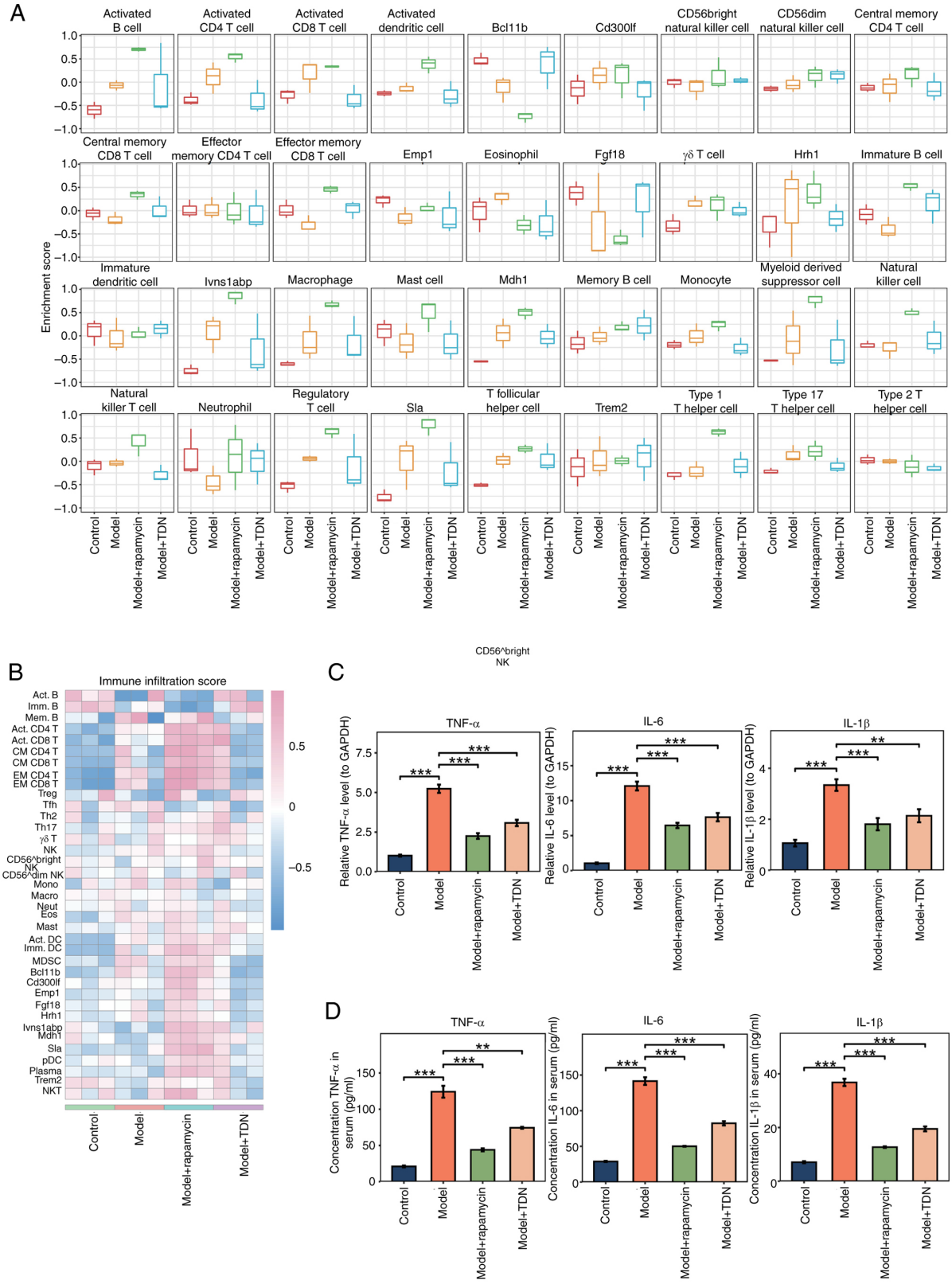


Figure 4. (A) Immune infiltration score boxplot. Single-sample gene set enrichment analysis was used to calculate the immune cell infiltration scores in each group and results were displayed as a boxplot, with the box representing the interquartile range, the median indicated by a horizontal line and the whiskers showing the distribution range of the data. (B) Immune infiltration score heatmap. After standardization, the heatmap displays the infiltration scores of different immune cells across groups. Color changes represent high to low immune infiltration scores, with red indicating high scores and blue indicating low scores, rows represent different immune cell types, and columns represent experimental groups. (C) RT-qPCR detection of inflammatory cytokines. RT-qPCR analysis was used to measure the mRNA expression levels of IL-6, IL-1β and TNF-α. $^{**}$P<0.01 and $^{***}$P<0.001. (D) ELISA detection of inflammatory cytokines in serum. An ELISA was used to measure the levels of IL-6, IL-1β and TNF-α in serum. $^{**}$P<0.01 and $^{***}$P<0.001. RT-qPCR, reverse transcription-quantitative PCR; TDN, tetrahedral DNA nanostructure; NK, natural killer; NKT, natural killer T cell; DC, dendritic cell; pDC, plasmacytoid dendritic cell; MDSC, myeloid-derived suppressor cell; Act., activated; Imm., immature; CM, central memory; EM, effector memory; Treg, regulatory T cell; Tfh, T follicular helper cell; Th1, type 1 T helper cell; Th2, type 2 T helper cell; Th17, type 17 T helper cell; Mono, monocyte; Macro, macrophage; Neut, neutrophil; Eos, eosinophil; Mast, mast cell; Plasma, plasma cell.

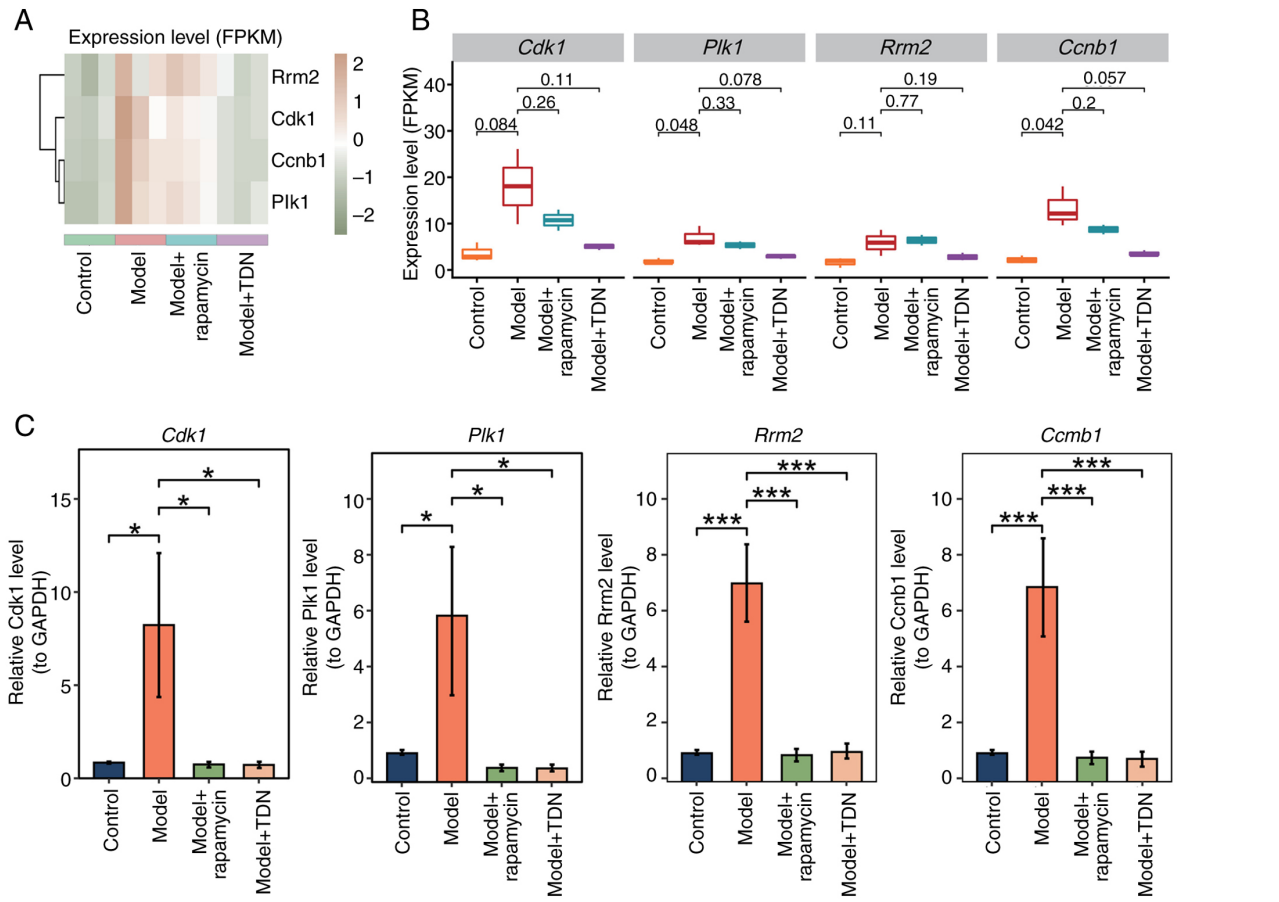


Figure 5. (A) Gene expression heatmap and (B) boxplots for *Ccnb1, Rrm2, Plk1* and *Cdk1*. The heatmap shows the expression level changes of *Ccnb1, Rrm2, Plk1* and *Cdk1* across groups, with color changes reflecting the difference in gene expression, where orange indicates high expression and green indicates low expression. The boxplot illustrates the distribution of gene expression levels among groups. (C) RT-qPCR detection of gene expression. RT-qPCR was used to measure the mRNA expression levels of *Ccnb1, Rrm2, Plk1* and *Cdk1* in urethral tissue, with results displayed in a bar chart. $^{*}$P<0.05 and $^{***}$P<0.001. RT-qPCR, reverse transcription-quantitative PCR; TDN, tetrahedral DNA nanostructure; *Ccnb1*, cyclin B1; *Rrm2*, ribonucleotide reductase regulatory subunit M2; *Plk1*, polo-like kinase 1; *Cdk1*, cyclin-dependent kinase 1; *FPKM*, fragments per kilobase million.

(Actg1), may have promoted cell proliferation and migration at the injury site, thereby facilitating tissue repair after urethral injury. Regulation of cell proliferation and migration is a critical step in the tissue repair process, as it directly influences cellular turnover and structural remodeling during wound healing (28), and changes in gene expression in this module may reflect the activation of repair-associated cellular programs. *Cellular stress response*. Genes involved in cellular stress responses, such as peroxiredoxin 1, and heat shock protein family A member 5, may have helped cells to cope with injury and maintain normal function by regulating stress responses. The regulation of stress responses is important for cell survival and functional recovery after injury (27).

After urethral injury, activation of the immune response was supported by the differential expression of genes, such as *IL-1β*, *C1qa* and *C1qb*, suggesting that the immune response may have served an important role in the repair process. The immune system may have regulated inflammation and served a key role in fibrosis and tissue repair. Differential expression of *Cd68* and *Actg1* suggested that cell proliferation and migration served key roles in the repair process after injury. Changes in the expression of genes involved in cell energy metabolism, such as *Pgk1* and *Ldha*, suggested that cell metabolism was important for repair after injury by providing sufficient energy

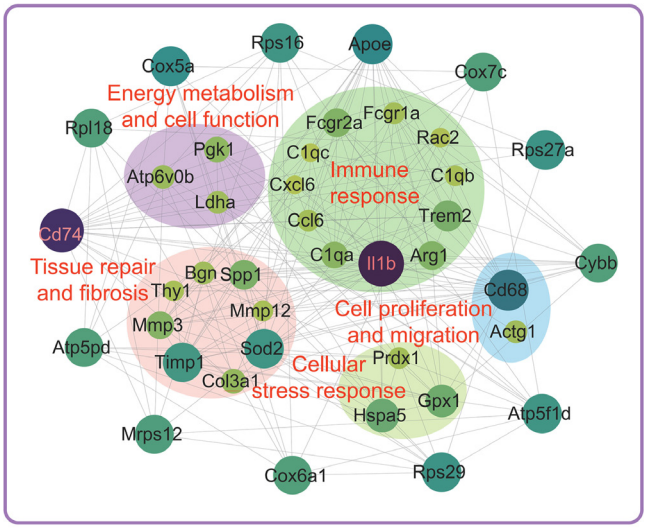


Figure 6. Differential gene network analysis. The nodes represent differentially expressed genes across the four groups, and the edges represent the interactions between these genes. The network analysis involved multiple biological processes, including tissue repair and fibrosis, cell proliferation and migration, energy metabolism and cell function, immune response and cellular stress response. Each node represents an individual differentially expressed gene in the network, and the depth of the color of the node reflects the frequency of gene interaction in the network. The darker the color, the more frequently the gene participates in interactions.

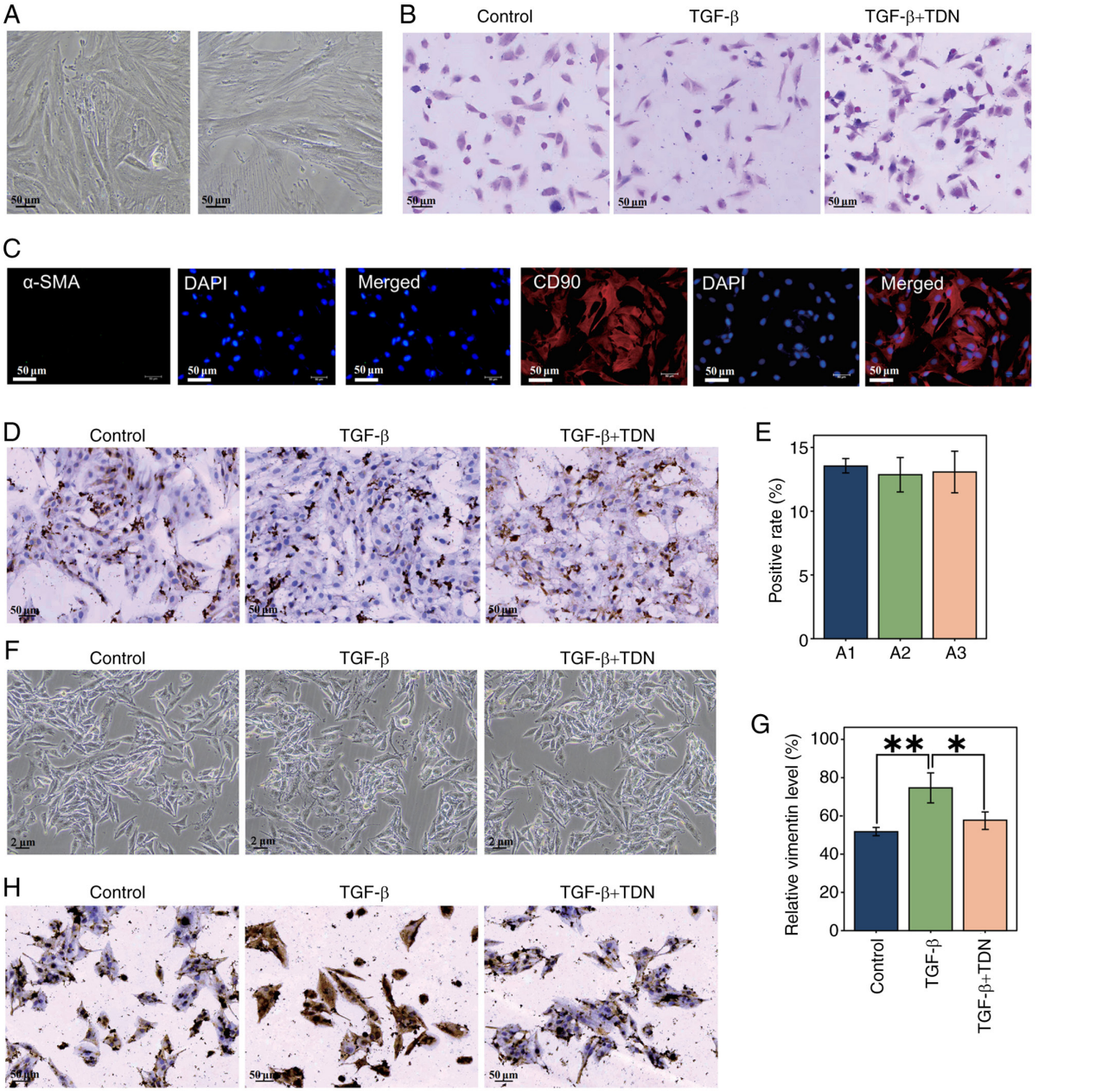


Figure 7. (A) Fibroblast isolation and cultivation. Representative phase-contrast images of primary rat urethral fibroblasts following enzymatic digestion are shown. The two images represent different microscopic fields from the same primary culture, illustrating progressive cell adhesion and the typical spindle-shaped, adherent morphology with elongated cell bodies and prominent cytoplasmic extensions. (B) H&E staining. Cell nuclei were stained darkly, with the cytoplasm stained lightly and clear cell boundaries visible, with cells displaying the normal morphological characteristics of fibroblasts after H&E staining. (C) Immunofluorescence staining identification of fibroblasts. Immunofluorescence staining for α-SMA (green) and CD90 (red) was performed to verify fibroblast purity. Nuclei were counterstained with DAPI (blue) and imaged at a magnification of x200 using a Nikon TS2-S-SM fluorescence microscope. Cells exhibited strong CD90 expression, α-SMA staining was negative, whereas CD90 staining was clearly positive, confirming fibroblast identity and excluding myofibroblast contamination. (D) Immunohistochemical detection of vimentin. Vimentin expression in fibroblasts was detected by immunohistochemistry. The nuclei were stained blue, and vimentin-positive cytoplasm appeared brownish-yellow. Images were obtained at a magnification of x200 using a digital slide scanner. (E) Immunohistochemical detection of vimentin. Quantitative analysis among three replicates was performed using Image-Pro Plus, and statistical evaluation with GraphPad Prism 9.0 showed no significant differences among groups ($P>0.05$), confirming reproducibility. (F) Cell culture under different treatments. Representative phase-contrast images (magnification, x100) showed fibroblasts in the control, TGF-β and TGF-β + TDN groups, all displaying sufficient adherence and morphology. (G) Quantitative analysis of vimentin expression under different treatments. Vimentin expression levels in fibroblasts from the control, TGF-β and TGF-β + TDN groups were quantified based on immunohistochemical staining using Image-Pro Plus. Statistical analysis was performed using GraphPad Prism 9.0 ($^{*}P<0.05$, $^{**}P<0.01$). (H) Immunohistochemical detection of vimentin under different treatments. Representative immunohistochemical images showed vimentin expression in fibroblasts from the Control, TGF-β and TGF-β + TDN groups. α-SMA, α-smooth muscle actin; TDN, tetrahedral DNA nanostructure.

to support cellular activities involved in tissue repair. The differential expression of genes associated with fibrosis, such as *Bgn* and *Mmp3*, suggested that fibrosis may have occurred after urethral injury and affected tissue repair.

*Effect of TDN on vimentin expression*. To explore the effect of TDN on vimentin expression, fibroblasts were successfully isolated from rat urethral tissue and cultured using an enzymatic digestion method. The cells exhibited typical adherent

growth characteristics (Fig. 7A). H&E staining revealed that these fibroblasts displayed typical morphological features, including deeply stained nuclei, lightly stained cytoplasm and clearly defined cell boundaries (Fig. 7B). To ensure the purity of fibroblasts used for vimentin regulation assays, immunofluorescence staining of α-SMA and CD90 was performed. Cells exhibited negative α-SMA staining together with positive CD90 expression, confirming fibroblast identity and excluding myofibroblast contamination (Fig. 7C). Immunohistochemical analysis showed high expression of vimentin in all three repeats (Fig. 7D and E).

Subsequently, three experimental conditions were established: Control, TGF-β-induced vimentin expression and TGF-β-induced vimentin expression + TDN treatment. Cells showed satisfactory growth in all groups (Fig. 7F). Immunohistochemical analysis was conducted to detect vimentin expression after different treatments. Cell images showed that the nuclei were stained blue, with vimentin stained brownish-yellow (Fig. 7H). Quantitative analysis indicated that, compared with the control group, treatment with TGF-β significantly increased the expression of vimentin ($P<0.01$). Treatment with TDN significantly reduced the expression of vimentin compared with that in the TGF-β group ($P<0.05$) (Fig. 7G). These results suggested that TDN may have regulated urethral fibrosis by inhibiting TGF-β-induced expression of vimentin.

## Discussion

In the present study, a rat model of urethral injury was successfully established, and the therapeutic effects of rapamycin and TDN on urethral injury, fibrosis and the immune response were evaluated. The results indicated that TDN markedly alleviated urethral injury, inhibited the progression of fibrosis and modulated immune responses, highlighting its potential as a therapeutic agent. The key findings and their possible mechanisms are discussed subsequently.

In the present study, a rat model of urethral injury was established using a mechanical method closely mimicking traumatic urethral injury and allowing precise control of the injury (27,39). The model was validated by multiple indicators, including retrograde urethral angiography, H&E staining and pathological analysis. These methods confirmed urethral stenosis, fibrosis and inflammatory infiltration in the model group. Both Rapamycin and TDN notably improved pathological changes, supporting the reliability of the model.

Excessive immune activation is an important driver of fibrosis after urethral injury (40-42). Transcriptomic analysis and RT-qPCR revealed increased immune cell infiltration and elevated levels of the pro-inflammatory cytokines IL-6, IL-1β and TNF-α in the model group (10). Treatment with TDN significantly reduced cytokine expression and immune cell infiltration, indicating effective immunomodulation. Pathway enrichment analysis also suggested that TDN suppressed the 'NF-κB signaling pathway', 'NOD-like receptor signaling pathway' and 'Cytokine-cytokine receptor interaction' (43-47), thereby attenuating immune-inflammatory responses. TDN mitigated excessive inflammation and fibrosis by limiting macrophage and T-cell infiltration (48-50).

Fibrosis is the predominant cause of urethral stenosis and dysfunction (51). In the present study, TDN significantly reduced collagen deposition and the expression of fibrosis markers, including α-SMA, collagen I/III and Smad3, compared with that in the model group. Transcriptomic analyses indicated that TDN may have prevented the progression of fibrosis via pathways associated with cellular metabolism and fibroblast activation. The altered expression levels of *Pgk1* and *Ldha* suggested that TDN improved energy metabolism to support repair (52,53), while changes in *Cd74*, *Bgn* and *Mmp3* implied direct regulation of fibrosis-associated genes (54,55). Inhibition of TGF-β-induced vimentin expression supported the anti-fibrotic potential of TDN (56).

Tissue repair after urethral injury necessitates balanced cell proliferation (57-59). Aberrant upregulation of cell cycle genes, such as *Ccnb1*, *Rrm2*, *Plk1* and *Cdk1*, may enhance tissue fibrosis (60,61). Treatment with TDN significantly reduced the expression of some of these genes, whereas others showed a decreasing trend, thereby preventing excessive fibroblast proliferation and limiting collagen deposition. Furthermore, by improving energy metabolism via genes such as *Pgk1* and *Ldha*, TDN indirectly modulated the cell cycle and maintained controlled proliferation (52,62,63).

Immune responses serve both protective and pathogenic roles in fibrosis (41). In the present study, transcriptomic analysis revealed excessive activation of immune-related genes, including *Il-1β*, *C1qa* and *C1qb*, indicating excessive activation of pro-inflammatory and complement-associated immune responses in the model group., consistent with previous reports showing that immune activation contributes to fibrosis (40,50,64). TDN downregulated pro-inflammatory cytokines, such as IL-6 and TNF-α, and prevented immune cell infiltration, thereby attenuating fibrosis-promoting immune reactions (41,65-68). These findings suggested that the anti-fibrotic effects of TDN were closely linked to its immunomodulatory properties.

Although TDN showed significant therapeutic efficacy in the rat model, further studies are needed to confirm its potential for clinical application. Additionally, the present study primarily focused on immune regulation and the inhibition of fibrosis. Future studies should further investigate the effects of TDN on specific immune cell subtypes, such as macrophage polarization states (M1/M2) and distinct lymphocyte subsets, using more targeted experimental approaches, including flow cytometry, immunofluorescence co-staining and single-cell RNA sequencing. Additionally, future work may explore potential synergistic applications of TDN with other therapeutic agents. In summary, the present study revealed that TDN promoted repair after urethral injury by regulating immune responses, suppressing fibrosis and improving cellular metabolism. These findings not only highlight the value of TDN as a promising therapeutic candidate for urethral injury but also provide novel insights into immunoregulatory strategies for fibrotic diseases.

## Acknowledgements

Not applicable.

## Funding

The present research was funded by the Guizhou Provincial Natural Science Foundation [grant no. Qiankehebasis-ZK

(2024) general 241], the Start-up Fund for Doctoral Research at the Affiliated Hospital of Guizhou Medical University (grant no. gyfybsky-2022-38), the National Natural Science Foundation of China Cultivation Program of Affiliated Hospital of Guizhou Medical University [grant no. gyfynsfc (2023)-62], the Key Medical Discipline Construction Project of Guizhou Provincial Health Commission during 2025-2026 and the 2025 Annual Hospital-Level Scientific Research Fund of Guizhou Hospital of Beijing Jishuitan Hospital [grant no. JGYYK(2025)-24].

## Availability of data and materials

The RNA sequencing data generated in the present study have been deposited in the NCBI Gene Expression Omnibus (GEO) database under accession number GSE314890 or at the following URL: https://www.ncbi.nlm.nih.gov/geo/query/acc.cgi?acc=GSE314890. The raw sequencing data (FASTQ files) have been submitted to the NCBI Sequence Read Archive under BioProject accession number PRJNA1393091 or at the following URL: https://www.ncbi.nlm.nih.gov/bioproject/PRJNA1393091. Other data generated in this study are available from the corresponding author upon reasonable request.

## Authors' contributions

CG conceived and designed the experiments, performed the experiments, analyzed the data and drafted the manuscript. JL contributed to the conceptualization and experimental design of the study, critically interpreted the data, revised the manuscript for important intellectual content, supervised the research process and secured funding. CG and JL confirm the authenticity of all the raw data. All authors read and approved the final manuscript.

## Ethics approval and consent to participate

The present study was approved by the Experimental Animal Welfare and Ethics Committee of Guizhou Medical University (Guiyang, China; approval no. 2502311).

## Patient consent for publication

Not applicable.

## Competing interests

The authors declare that they have no competing interests.

## References

1. Mundy AR and Andrich DE: Urethral trauma. Part I: Introduction, history, anatomy, pathology, assessment and emergency management. BJU Int 10: 310-327, 2011.
2. Rosenstein DI and Alsikafi NF: Diagnosis and classification of urethral injuries. Urol Clin North Am 33: 73-85, 2006.
3. Verla W, Oosterlinck W, Spinoit AF and Waterloos M: A comprehensive review emphasizing anatomy, etiology, diagnosis, and treatment of male urethral stricture disease. Biomed Res Int 2019: 9046430, 2019.
4. Payne SR, Anderson P, Spasojević N, Demilow TL, Teferi G and Dickerson D: Male urethral stricture disease: Why management guidelines are challenging in low-income countries. BJU Int 130: 157-165, 2022.
5. Rahardjo HE, Märker V, Tsikas D, Kuczyk MA, Ückert S and Bannowsky A: Fibrotic strategies diseases of the human urinary and genital tract: Current understanding and potential for treatment. J Clin Med 12: 4770, 2023.
6. Doersch KM, Barnett D, Chase A, Johnston D and Gabrielsen JS: The contribution of the immune system to genitourinary fibrosis. Exp Biol Med (Maywood) 247: 765-778, 2022.
7. Metcalfe PD, Wang J, Jiao H, Huang Y, Hori K, Moore RB and Tredget EE: Bladder outlet obstruction: Progression from inflammation to fibrosis. BJU Int 106: 1686-1694, 2010.
8. Hirano Y, Horiguchi A, Ojima K, Azuma R, Shinchi M, Ito K and Miyai K: Myofibroblast-dominant proliferation associated with severe fibrosis in bulbar urethral strictures. Int J Urol 30: 107-112, 2023.
9. Wynn TA: Cellular and molecular mechanisms of fibrosis. J Pathol 214: 199-210, 2008.
10. Lupher ML Jr and Gallatin WM: Regulation of fibrosis by the immune system. Adv Immunol 89: 245-288, 2006.
11. Tiwari P, Verma S, Washimkar KR and Nilakanth Mugale M: Immune cells crosstalk Pathways, and metabolic alterations in Idiopathic pulmonary fibrosis. Int Immunopharmacol 135: 112269, 2024.
12. Cangemi M: Multiparametric immune profiling to predict the risk of cancer development in chronic immune suppressed solid organ transplant patients. (Doctoral dissertation, University of Udine), 2019.
13. Gedaly R, De Stefano F, Turcios L, Hill M, Hidalgo G, Mitov MI, Alstott MC, Butterfield DA, Mitchell HC, Hart J, *et al*: mTOR inhibitor everolimus in regulatory T cell expansion for clinical application in transplantation. Transplantation 103: 705-715, 2019.
14. Blagosklonny MV: Rapamycin for longevity: Opinion article. Aging (Albany NY) 11: 8048-8067, 2019.
15. Stallone G, Infante B, Grandaliano G and Gesualdo L: Management of side effects of sirolimus therapy. Transplantation 87 (8 Suppl): S23-S26, 2009.
16. Li J, Kim SG and Blenis J: Rapamycin: One drug, many effects. Cell Metab 19: 373-379, 2014.
17. Keller A and Linko V: Challenges and perspectives of DNA nanostructures in biomedicine. Angew Chem Int Ed Engl 59: 15818-15833, 2020.
18. Györfi AH, Matei AE and Distler JHW: Targeting TGF-β signaling for the treatment of fibrosis. Matrix Biol 68-69: 8-27, 2018.
19. Zhao X, Kwan JYY, Yip K, Liu PP and Liu FF: Targeting metabolic dysregulation for fibrosis therapy. Nat Rev Drug Discov 19: 57-75, 2020.
20. Wang W, Lin M, Wang W, Shen Z and Wu S: DNA tetrahedral nanostructures for the biomedical application and spatial orientation of biomolecules Bioactive Materials 33: 279-310, 2024.
21. Zhang Q, Jiang Q, Li N, Dai L, Liu Q, Song L, Wang J, Li Y, Tian J, Ding B and Du Y: DNA origami as an in vivo drug delivery vehicle for cancer therapy. ACS Nano 8: 6633-6643, 2014.
22. Shi S, Lin S, Shao X, Li Q, Tao Z and Lin Y: Modulation of chondrocyte motility by tetrahedral DNA nanostructures. Cell Proliferation 50: e12368, 2017.
23. Hong S, Jiang W, Ding Q, Lin K, Zhao C and Wang X: The Current Progress of Tetrahedral DNA Nanostructure for Antibacterial Application and Bone Tissue Regeneration. Int J Nanomedicine 18: 3761-3780, 2023.
24. Gu J, Liang J, Tian T and Lin Y: Current Understanding and Translational Prospects of Tetrahedral Framework Nucleic Acids. JACS 5: 486-520, 2025.
25. Liang S, Li J, Zou Z, Mao M, Ming S, Lin F, Zhang Z, Cao, Cao C, Zhou J, *et al*: Tetrahedral DNA nanostructures synergize with $MnO_2$ to enhance antitumor immunity via promoting STING activation and M1 polarization. Acta Pharmaceutica Sinica B 12: 2494-2505, 2022.
26. Cui W, Yang X, Dou Y, Du Y, Ma X, Hu L and Lin Y: Effects of tetrahedral DNA nanostructures on the treatment of osteoporosis. Cell Proliferation 57: e13625, 2024.
27. Wu Z, Tang Z, Zheng Z and Tan S: A novel trauma induced urethral stricture in rat model. Sci Rep 14: 6325, 2024.
28. Hyuga T, Fujimoto K, Hashimoto D, Tanabe K, Kubo T, Nakamura S, Ueda Y, Fujita-Jimbo E, Muramatsu K, Suzuki K, *et al*: Wound healing responses of urinary extravasation after urethral injury. Sci Rep 13: 10628, 2023.
29. She L, Niu B, Wu X, Yin Y, Wen K, Li H, Xie D, Zheng X and Dai Y: Iatrogenic injury recapitulated: Electroexcision technique for urethral stricture modeling in rats. J Vis Exp 212: 66864, 2024.

30. Abdelkhalek AS, Clarke PD, Sommers MA, Oe T, Andersen TM, Andersen CT, Hejbøl EK, Schrøder HD and Zvara P: Validation of a new rat model of urethral sphincter injury and leak point pressure measurements. Scand J Urol 55: 498-504, 2021.
31. Aydın A, Sönmez MG, Oltulu P, Kocabaş R, Öztürk Sönmez L, Özcan S, Boğa MS and Balasar M: Histopathologic evaluation of the effects of intraurethral platelet rich plasma in urethral trauma experimentally induced in rat model. Urology 141: 187.e9-187.e14, 2020.
32. Zhang SL and Wong AW: A novel technique for atraumatic transurethral catheterisation of male rats. Biol Open 13: bio060476, 2024.
33. Bauman TM, Nicholson TM, Abler LL, Eliceiri KW, Huang W, Vezina CM and Ricke WA: Characterization of fibrillar collagens and extracellular matrix of glandular benign prostatic hyperplasia nodules. PLoS One 9: e109102, 2014.
34. Shen H, Wang J, Min J, Xi W, Gao Y, Yin L, Yu Y, Liu K, Xiao J, Zhang YF and Wang ZN: Activation of TGF-β1/α-SMA/Col I profibrotic pathway in fibroblasts by galectin-3 contributes to atrial fibrosis in experimental models and patients. Cell Physiol Biochem 47: 851-863, 2018.
35. Taylor SC and Posch A: The design of a quantitative western blot experiment. Biomed Res Int 2014: 361590, 2014.
36. Modi A, Vai S, Caramelli D and Lari M: The Illumina sequencing protocol and the NovaSeq 6000 system. Methods Mol Biol 2242: 15-42, 2021.
37. Livak KJ and Schmittgen TD: Analysis of relative gene expression data using real-time quantitative PCR and the 2(-Delta Delta C(T)) method. Methods 25: 402-408, 2001.
38. Bindea G, Mlecnik B, Tosolini M, Kirilovsky A, Waldner M, Obenauf AC, Angell H, Fredriksen T, Lafontaine L, Berger A, *et al*: Spatiotemporal dynamics of intratumoral immune cells reveal the immune landscape in human cancer. Immunity 39: 782-795, 2013.
39. Ergün O, Tepebaşi MY, Onaran İ, Öztürk SA, Baltik M and Koşar PA: Standardizing urethral stricture models in rats: A comprehensive study on histomorphologic and molecular approach. Int Urol Nephrol 56: 2945-2954, 2024.
40. Antar SA, Ashour NA, Marawan ME and Al-Karmalawy AA: Fibrosis: Types, effects, markers, mechanisms for disease progression, and its relation with oxidative stress, immunity, and inflammation. Int J Mol Sci 24: 4004, 2023.
41. Huang E, Peng N, Xiao F, Hu D, Wang X and Lu L: The roles of immune cells in the pathogenesis of fibrosis. Int J Mol Sci 21: 5203, 2020.
42. Ising C and Heneka MT: Functional and structural damage of neurons by innate immune mechanisms during neurodegeneration. Cell Death Dis 9: 120, 2018.
43. Qiu D, Zhang D, Yu Z, Jiang Y and Zhu D: Bioinformatics approach reveals the critical role of the NOD-like receptor signaling pathway in COVID-19-associated multiple sclerosis syndrome. J Neural Transm (Vienna) 129: 1031-1038, 2022.
44. Tieri P, Termanini A, Bellavista E, Salvioli S, Capri M and Franceschi C: Charting the NF-κB pathway interactome map. PLoS One 7: e32678, 2012.
45. Shawky E, Nada AA and Ibrahim RS: Potential role of medicinal plants and their constituents in the mitigation of SARS-CoV-2: Identifying related therapeutic targets using network pharmacology and molecular docking analyses. RSC Adv 10: 27961-27983, 2020.
46. Wang M, Li X, Yang Z, Chen Y, Shu T and Huang Y: LncRNA MEG3 alleviates interstitial cystitis in rats by upregulating Nrf2 and inhibiting the p38/NF-κB pathway. Cytokine 165: 156169, 2023.
47. Naiyila X, Li J, Huang Y, Chen B, Zhu M, Li J, Chen Z, Yang L, Ai J, Wei Q, *et al*: A novel insight into the immune-related interaction of inflammatory cytokines in benign prostatic hyperplasia. J Clin Med 12: 1821, 2023.
48. Barron L and Wynn TA: Fibrosis is regulated by Th2 and Th17 responses and by dynamic interactions between fibroblasts and macrophages. Am J Physiol Gastrointest Liver Physiol 300: G723-G728, 2011.
49. Zhang M and Zhang S: T cells in fibrosis and fibrotic diseases. Front Immunol 11: 1142, 2020.
50. Wynn TA and Barron L: Macrophages: Master regulators of inflammation and fibrosis. Semin Liver Dis 30: 245-257, 2010.
51. Lima NA, Vasconcelos CC, Filgueira PH, Kretzmann M, Sindeaux TA, Feitosa Neto B, Silva Junior GB and Daher EF: Review of genitourinary tuberculosis with focus on end-stage renal disease. Rev Inst Med Trop Sao Paulo 54: 57-60, 2012.
52. Gou R, Hu Y, Liu O, Dong H, Gao L, Wang S, Zheng M, Li X and Lin B: PGK1 is a key target for anti-glycolytic therapy of ovarian cancer: Based on the comprehensive analysis of glycolysis-related genes. Front Oncol 11: 682461, 2021.
53. Wang P, Wang Q, Yang X, An Y, Wang J, Nie F, Pan B, Bi H and Qin Z: Targeting the glycolytic enzyme PGK1 to inhibit the warburg effect: A new strategy for keloid therapy. Plast Reconstr Surg 151: 970e-980e, 2023.
54. Lv W, Wu M, Ren Y, Luo X, Hu W, Zhang Q and Wu Y: Treatment of keloids through Runx2 siRNA-induced inhibition of the PI3K/AKT signaling pathway. Mol Med Rep 23: 55, 2021.
55. Giannandrea M and Parks WC: Diverse functions of matrix metalloproteinases during fibrosis. Dis Model Mech 7: 193-203, 2014.
56. Cheng F, Shen Y, Mohanasundaram P, Lindström M, Ivaska J, Ny T and Eriksson JE: Vimentin coordinates fibroblast proliferation and keratinocyte differentiation in wound healing via TGF-β-Slug signaling. Proc Natl Acad Sci USA 113: E4320-E4327, 2016.
57. Diaz-Moralli S, Tarrado-Castellarnau M, Miranda A and Cascante M: Targeting cell cycle regulation in cancer therapy. Pharmacol Ther 138: 255-271, 2013.
58. Campos A and Clemente-Blanco A: Cell cycle and DNA repair regulation in the damage response: Protein phosphatases take over the reins. Int J Mol Sci 21: 446, 2020.
59. Vermeulen K, Van Bockstaele DR and Berneman ZN: The cell cycle: A review of regulation, deregulation and therapeutic targets in cancer. Cell Prolif 36: 131-149, 2003.
60. Baek A, Shin JC, Lee MY, Kim SH, Kim J and Cho SR: Parasympathetic effect induces cell cycle activation in upper limbs of paraplegic patients with spinal cord injury. Int J Mol Sci 20: 5982, 2019.
61. Darby IA and Hewitson TD: Hypoxia in tissue repair and fibrosis. Cell Tissue Res 365: 553-562, 2016.
62. Icard P, Fournel L, Wu Z, Alifano M and Lincet H: Interconnection between metabolism and cell cycle in cancer. Trends Biochem Sci 44: 490-501, 2019.
63. He Y, Luo Y, Zhang D, Wang X, Zhang P, Li H, Ejaz S and Liang S: PGK1-mediated cancer progression and drug resistance. Am J Cancer Res 9: 2280-2302, 2019.
64. Absinta M, Maric D, Gharagozloo M, Garton T, Smith MD, Jin J, Fitzgerald KC, Song A, Liu P, Lin JP, *et al*: A lymphocyte-microglia-astrocyte axis in chronic active multiple sclerosis. Nature 597: 709-714, 2021.
65. Wick G, Grundtman C, Mayerl C, Wimpissinger TF, Feichtinger J, Zelger B, Sgonc R and Wolfram D: The immunology of fibrosis. Annu Rev Immunol 31: 107-135, 2013.
66. Gieseck RL III, Wilson MS and Wynn TA: Type 2 immunity in tissue repair and fibrosis. Nat Rev Immunol 18: 62-76, 2018.
67. Möller B and Villiger PM: Inhibition of IL-1, IL-6, and TN Semin Immunopathol 27: 391-408, 2006.
68. Wang T and He CJ: TNF-α and IL-6: The link between immune and bone system. Curr Drug Targets 21: 213-227, 2020.